INTERNATIONAL SOCIETY FOR SOIL MECHANICS AND GEOTECHNICAL ENGINEERING

SIMSG   ISSMGE

Subsoil stiffness effects on the bridge-abutment dynamic behaviour

Yazan B. Asia[1][#] and *Gopal S.P.* Madabhushi[1]

[1]*Schofield Centre, Department of Engineering, University of Cambridge, Cambridge, UK*
[#]*Corresponding author: ybya2@cam.ac.uk*

ABSTRACT

Integral abutment bridges (IABs) are robust structures that avoid the use of bearings and expansion joints and are relatively maintenance-free compared to conventional bridges. The seismic design code of IABs is not fully developed, and the complex soil-abutment interaction is not well understood. Therefore, research was carried out at the Schofield centre, the University of Cambridge, to understand the backfill-abutment interaction under earthquake loading, aimed at developing design guidelines for the industry. Understanding the mechanics by which the foundation soil stiffness and strength govern the abutment deformation and, thus, the earth pressures generated behind the abutment is essential. Two centrifuge tests have been conducted simulating an abutment with the conventional abutment-deck connection (or semi-integral abutment bridge), where moment restraint is released. In this paper, the dynamic response of the abutment founded on dry and liquefiable sandy soil is compared. Different deformation modes have been observed depending on the relative abutment-soil stiffness. The abutment experienced minimal base displacement in dry sands. Conversely, the abutment witnessed cyclic rotational ratcheting about the deck level in liquefiable soil. The dry soil test helped identify the zones where soil stiffness and strength loss can be critical. In the case of the saturated test, the water table level was up to one-third of the abutment height, fully saturating the foundation soil while the backfill height was dry. The comparative results highlight the vulnerability of semi-integral abutment walls to liquefaction-induced failure, as witnessed in the 2011 Christchurch earthquakes.

Keywords: integral bridges; abutments; earthquake-induced liquefaction; soil stiffness degradation; centrifuge modelling.

1. Introduction

Resilient and sustainable infrastructure assists in reducing environmental hazards and help achieve UN Sustainability Development Goals (SDGs). Recently, the bridge stock has experienced a considerable increase in infrastructure development due to the benefits they create on socio-economic impact. However, they are earth-retained structures that must account for the main conceptual design considerations in geotechnical engineering due to the strong interaction with the surrounding soil. These considerations are serviceability limit state (SLS) and ultimate limit state (ULS).

Conventional bridges involve a deck connected to abutments through bearings and expansion joints along the bridge span. The critical objective of expansion joints is to accommodate concrete-related problems, such as creep and shrinkage. On the other hand, bearings can afford thermal expansion and contraction-induced deck movement and, thereby, do not deform the backfill soil because of this slow cyclic loading (Burke and Martin 2009). Nonetheless, transport agencies have claimed that costly maintenance requirements arise from three primary sources, differential abutment-deck settlement due to the heavy traffic loading, corrosion of bearings because of deicing chemicals used in snowy regions, and, more prominent, the earthquake-induced liquefaction failure of abutments due to the independent dynamic response of abutments and bridge deck (Jonathan and Alampalli 2000). As a result of the previously mentioned drawbacks of traditional bridges, the scheme of integral bridges has been introduced.

Integral abutment bridges (IABs) are novel civil engineering systems with a large loading capacity due to the combined stiffness and strength of abutments and soil. The omission of bearings and expansion joints in this engineering system has enhanced serviceability under slow and quick loading events. Furthermore, avoiding the mechanical disruption and corrosion of bearings has led to highly cost-effective systems in terms of construction, maintenance, and lifespan (Mitoulis 2020). Fig. 1 shows the salient differences between conventional and integral bridges.

Despite these advantages, the rigid body motion because of the rigid connection between abutments and the bridge deck has introduced higher kinematic and inertial interactions, which induce shear and volumetric deformation on the foundation and backfill soil. The soil, in turn, must equilibrate the system by causing earth pressure on abutments. However, the mechanics by which forces are exerted on abutments, besides understanding the soil deformation mechanism, has not been experimentally investigated yet. Additionally, the current design of IABs is only based on numerical tools (Erhan and Dicleli 2014). Consequently, this research has been carried out to understand this soil-structure

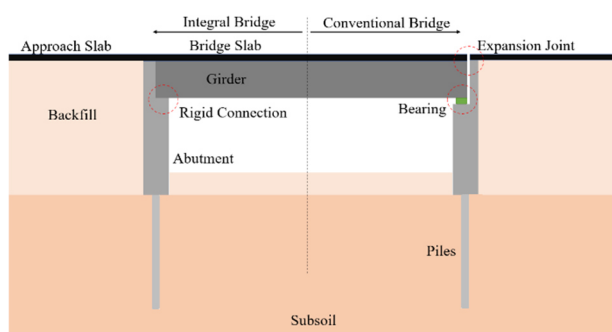interaction problem, aiming at developing guidelines for the industry.

Figure 1. The key features of a simplified geometry of integral and conventional bridges.

Two centrifuge tests were conducted at the Schofield Centre at the University of Cambridge to understand the seismic performance of stiff abutments. The tests conducted had similar testing configurations, with the key variation of fully saturated subsoil in one test and dry sandy soil in the other. That is to understand the subsoil stiffness effects on the relative soil-abutment movement, backfill deformation mechanism, and the dynamic response of soil and abutments. In these tests, the abutment-deck connection replicated the conventional and semi-integral abutment bridges, where no expansion gap is allowed but the rotational movement around the crest of the abutment is released. The reason is to gain a better insight into the influence of rotational fixity on the overall system dynamic response later in this research.

This paper compares the temporal dynamic response of a stiff abutment founded on dry and fully saturated subsoil. The corresponding generated excess +ve and -ve pore pressures following the contractile and dilative soil behaviour are also presented and directly synchronised to the attenuation or amplification of soil acceleration. In addition, the subsoil shear modulus variation with shear strain amplitude is estimated. The results from different instrumentation techniques are compared at a given instant to elucidate the overall mechanical behaviour and provide a better understanding.

When the abutment was founded on dry subsoil, the progressive cyclic straining of subsoil led to soil densification and locked-in stresses, and hence minimal relative soil-abutment displacement. In contrast, after positive excess pore pressure generation, the subsoil stiffness degradation induced irrecoverable abutment rotation, leading to earthquake-induced liquefaction failure.

2. Centrifuge Modelling

Over the last few decades, geotechnical centrifuge modelling has become popular in investigating the behaviour of geotechnical structures. The basic premise in centrifuge modelling is testing a scaled-down prototype in the increased field gravity. The enhanced g-field induces centrifugal acceleration varying across the depth of the model, ensuring that the stresses and strains at homologous depths in the prototype and model are identical. In this research, the Cambridge geotechnical

centrifuge has been utilised, which has a payload capacity of 1 ton accelerated at 150 times the earth's gravity (150 N). Schofield (1980) described the mechanics of models and the remoulded soil behaviour. Madabhushi (2014) described the scaling laws and the principles of using the 10 m Cambridge centrifuge installed at the Schofield Centre.

2.1. Prototype structure and model scaling

Several full-sized integral bridges are reported in the literature (Tubaldi et al. 2018). However, it is impractical to build the $1/N^{th}$ model replicating the real-field structure; therefore, the full-sized integral bridge has been simplified to a prototype structure capturing the essential behaviour of the field structure by considering the same mass and stiffness. The prototype structure is a 33.5 m single-span prestressed deck, and the transverse dimension of the bridge slab is 13.5 m, with the second moment of area of 5.0 m^4.

The prototype scenario was scaled down to fit the centrifuge model container with 720 × 250 × 400 mm dimensions, length, width, and depth. The g-level, by which the prototype structure was scaled and accelerated, considered the limitations and errors associated with the enhanced gravity testing described by Madabhushi (2014). Thus, a g level of 60 was ascertained at the third of soil height, where the centrifuge model and prototype stresses are precisely similar.

The prototype abutment length and the footing width were scaled directly by 1/N. However, these structural elements' bending stiffness must be considered to obtain the correct structural behaviour; according to this, the thickness of the abutment and footing was determined. It is worth highlighting that a 15% reduction for the prototype flexural stiffness was applied, accounting for cracks occurrence across its height. However, this assumption might be conservative as cracks only occur where the applied bending moment is higher than the design capacity at specific locations.

To meet the objectives of these two centrifuge tests, the bridge deck was simulated by a prop allowing rotational and vertical movement, as shown in Fig. 2. The design of this prop was optimised to minimise the deflection of this prop in the centrifugal acceleration direction. For ease of fabrication, aluminium alloy grade 6082-T6 was utilised in modelling the prototype structural elements. Table 1 summarises the prototype and model dimensions and material properties.

Table 1. Details of the prototype and model bridge.

	Prototype	Model
Concrete Modulus of elasticity	30 GPa	70 GPa
Abutment thickness	1.0 m	12.0 mm
Footing thickness	1.0 m	12.0 mm
Abutment height	9.0 m	150.0 mm
Footing width	6.0 m	100.0 mm

Figure 2 shows the dynamic centrifuge layout and the locations of instruments. The dimensions are in mm at model scale.
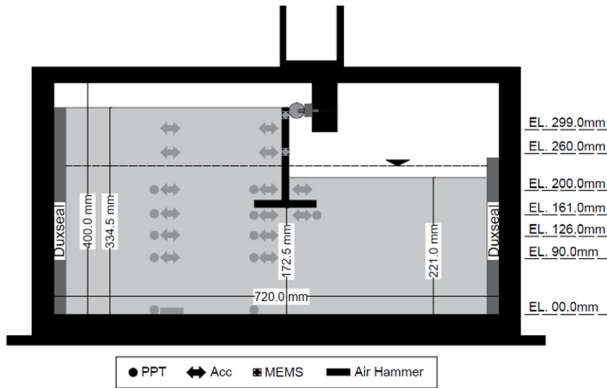

Figure 2. Centrifuge model layout (Dimensions in mm).

2.2. Model preparation

The centrifuge tests conducted involved a variety of miniature instrumentation techniques to acquire a better understanding of the soil and dynamic abutment behaviour. These are air hammer tool developed by Ghosh and Madabhushi (2002) to measure the in-flight shear wave (V_s) velocity during centrifuge tests, piezoelectric accelerometers (PIEZOs) to measure the soil acceleration, pore pressure transducers (PPTs) to measure the generated pore pressure, full Wheatstone bridges to capture the bending of the abutment, load cell to record the static and seismic-induced axial force on the bridge slab, micro-electro-mechanical system (MEMS) to measure the abutment acceleration, and tactile pressure sensing sheet manufactured by Tekscan to measure the effective horizontal stresses imposed on the abutment by the backfill soil. Duxseal blocks were placed at the edges of the centrifuge model box to minimise the propagation of P-waves (Steedman and Madabhushi 1990). However, in this paper, the results of the air hammer device and some MEMS, PPTs and PIEZOs are presented.

The schematic plan for both conducted tests was approximately similar to maintain a direct comparison between the instruments from both models at the exact location. A typical silica Hostun HN31 sand was used in these dynamic centrifuge tests. The soil relative density was maintained consistent and uniform across the depth of the model by using an automatic sand-pouring system installed at the Schofield centre. The basic premise of this system is based on maintaining the same flow rate and drop height during the sand pouring process. The drop height from the base of the 6 mm nozzle diameter to the surface of the soil layer was approximately 500 mm; this drop height is automatically maintained constant after pouring 7.5 mm of the soil layer. Further details can be found in (Madabhushi et al. 2006).

The water table level in the fully saturated soil model was up to the bottom third of the abutment height, so almost two-thirds of the backfill height was dry. The subsoil and backfill soil condition was dry in the other centrifuge model, illustrating the difference between the conducted tests. Fig. 3 shows the dry soil model's centrifuge package before the commencement of the seismic test. The centrifuge model container with the

Perspex window allows using a high-speed camera to track the soil movement.
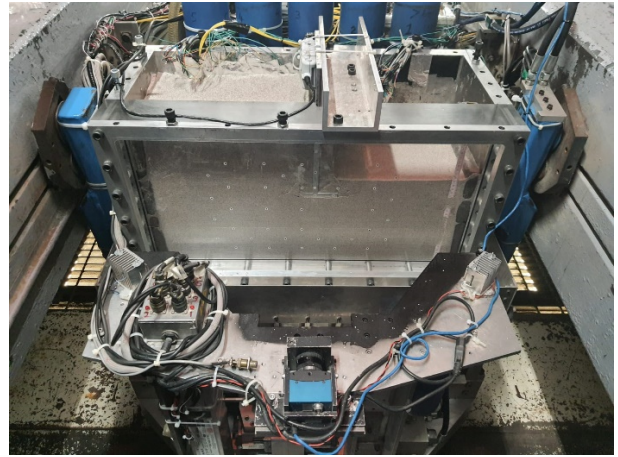

Figure 3. The dry soil model ready for testing.

Table 2 summarises the Hostun sand properties, following the work of (Shepley 2014). The soil relative density (I_d) in the dry soil model was 45%, whereas 32% in the saturated soil model; both are classified as loose sandy soil.

Table 2. Hostun HN31 sand properties.

	Value
Maximum density	1620 kg/m³
Minimum density	1308 kg/m³
Maximum void Ratio	1.01
Minimum void Ratio	0.555
Median grain size	338μm
Specific gravity	2.65

The saturated soil model was saturated using the Cam-Sat computer-controlled system developed by Stringer and Madabhushi (2009). The system can automatically control the vacuum gradients between the centrifuge model box and the reservoir of pore fluid, avoiding soil disturbance. For coupling of co-seismic and consolidation of the generated pore pressure with the time-scaling of the earthquake, hydroxypropyl methylcellulose (HPMC) was used to saturate the model. The substitute pore fluid had a viscosity 60 times the prototype pore fluid, water, prepared at the expected centrifuge chamber temperature (Stewart et al. 1998). Following two cycles of flushing the sealed centrifuge model container with CO_2, the high-viscosity fluid enters through vents in the base of the model box at a low flow rate of approximately 1.5 kg/hr. Fig. 4 shows the saturated soil model being saturated.
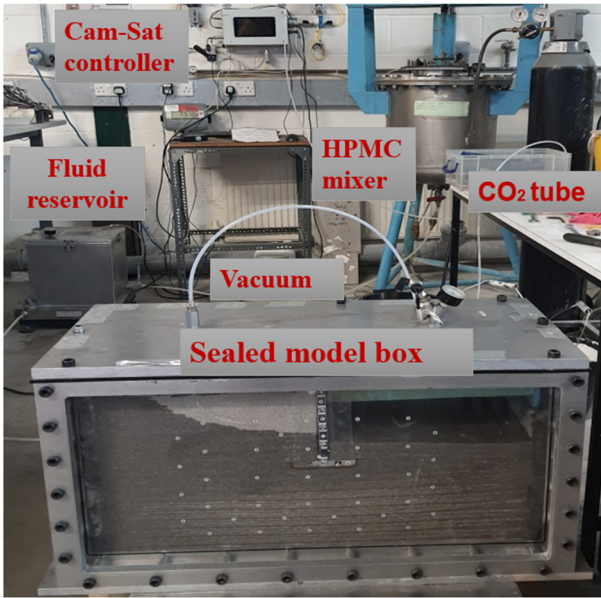
Figure 4. The centrifuge model box during saturation.

2.3. Testing plan

An identical testing plan was used for both centrifuge tests. The experimental centrifuge package was swung up to 60g, at which the geo-static soil stresses were recorded. After that, the centrifuge model was shaken by several earthquakes with different amplitudes and frequencies. The new servo-hydraulic shaker (Madabhushi et al. 2012) at the Schofield Centre was utilised to induce actual and sinusoidal earthquakes with single or multiple frequency contents. Nonetheless, the data from only two earthquakes are presented in this paper. The first earthquake is the scaled Kobe earthquake with a peak ground acceleration (PGA) of 0.22g and 2 Hz frequency, while the other is ten cycles of a sinusoidal wave with a PGA of 0.32g and a single frequency content of 1 Hz. The shear wave velocity, and hence the soil stiffness, were measured before and after each earthquake to investigate the soil stiffness variation. The soil shear modulus obtained from the air hammer tool was considered in this paper to examine the obtained soil stiffness values varied during the seismic event, calculated according to the process described in section 3.

3. Soil stiffness evaluation

The subsoil stiffness variation undoubtedly governs the mode and magnitude of abutment movements. The interpretation of soil shear modulus depends on the relative soil strain magnitude, confining pressure, and the nature of ground shaking (Hardin and Drnevich 1972b). In dry subsoil conditions, the soil stiffness might experience relative degradation at initial cycles of the input motion before stiffening again, depending on the soil state and the shear-induced volumetric strain. The soil hardening at that time may attract additional kinematic loads, mainly if the abutment was relatively stiff. However, loose sandy soil would witness considerable stiffness and strength degradation in saturated soil conditions due to their contractile nature

and very low permeability, which both assist in generating excess pore pressure. Positive pore pressures significantly lessen the effective stresses, causing failure of the abutment founded upon it (Haigh et al. 2012). Therefore, it is essential to get an insight into sandy soil's cyclic shear stress-shear strain behaviour and link this to the dynamic abutment response.

Soil stiffness variation during earthquake excitations can be evaluated using the soil acceleration time histories recorded by PIEZOs installed vertically at known depths (Zeghal and Elgamal 1994). Developing stress-strain loops and hence soil stiffness derivation has been popular among centrifuge modellers to understand the dry and saturated sandy soil response under dynamic loading.

The soil stiffness data presented here is obtained from five PIEZOs arranged in columns in two regions, the free and near fields. A critical step in the data processing of stress-strain loops is selecting appropriate data filtering. Higher harmonics of the main ground motion may exist. Thus, filtering them out would affect the derived soil response. The Fourier spectra for the unfiltered soil acceleration trace demonstrated the presence of higher harmonics in addition to the main driving frequency. Therefore, a bandpass filter at 0.3% and 7.5% of the sampling frequency (6000 Hz) is utilised in constructing the stress-strain loop; after each integration process of soil acceleration histories to eliminate strain drifting. The MATLAB zero-phase digital filtering (filtfilt) function is used with a Butterworth 8th order filter. It is essential to eliminate the low and high-frequency components, as the former cause drifts to the soil shear strain values, while the latter is considered noise.

The shear stress and strain values are evaluated using (Zeghal and Elgamal's 1994) expressions. Details about the process can be found in Brennan et al., 2005).

The evaluated soil stiffness variation with the relative induced shear strain is compared with the standard degradation curve (Hardin and Drnevich 1972a). The small-strain shear modulus (G_{max}) by which the cyclic soil stiffness values are usually normalised has been obtained from the shear wave velocity (V_s) measured by the air hammer tool, according to Eq. (1). Table 3 summaries the max soil stiffness obtained at a deeper depth where small shear strain is observed.

$$G_{max} = \rho \, V_S^2 \qquad (1)$$

Table 3. Small strain soil stiffness.

	Value
Dry soil model	133.0 MPa
Saturated soil model	60.0 MPa

4. Results and discussion

The results outlined herein are from large ground motions. The temporal variation of soil and abutment acceleration are presented and compared in Fig. 5. A simple schematic drawing indicates the instrument's location (red circle); the dashed black lines point out the Hostun sand soil level, while the dotted red line denotes the water table level in the saturated soil model. For both
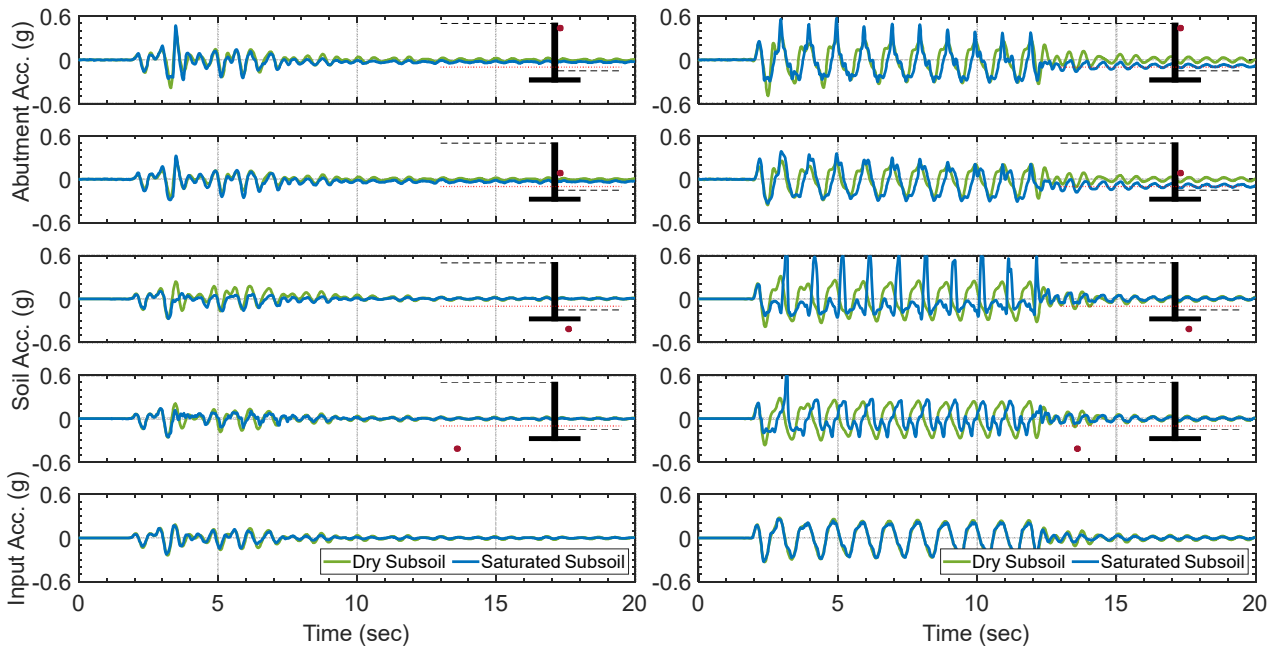
Figure 5. Soil and abutment acceleration histories recorded in the dry and saturated soil model tests
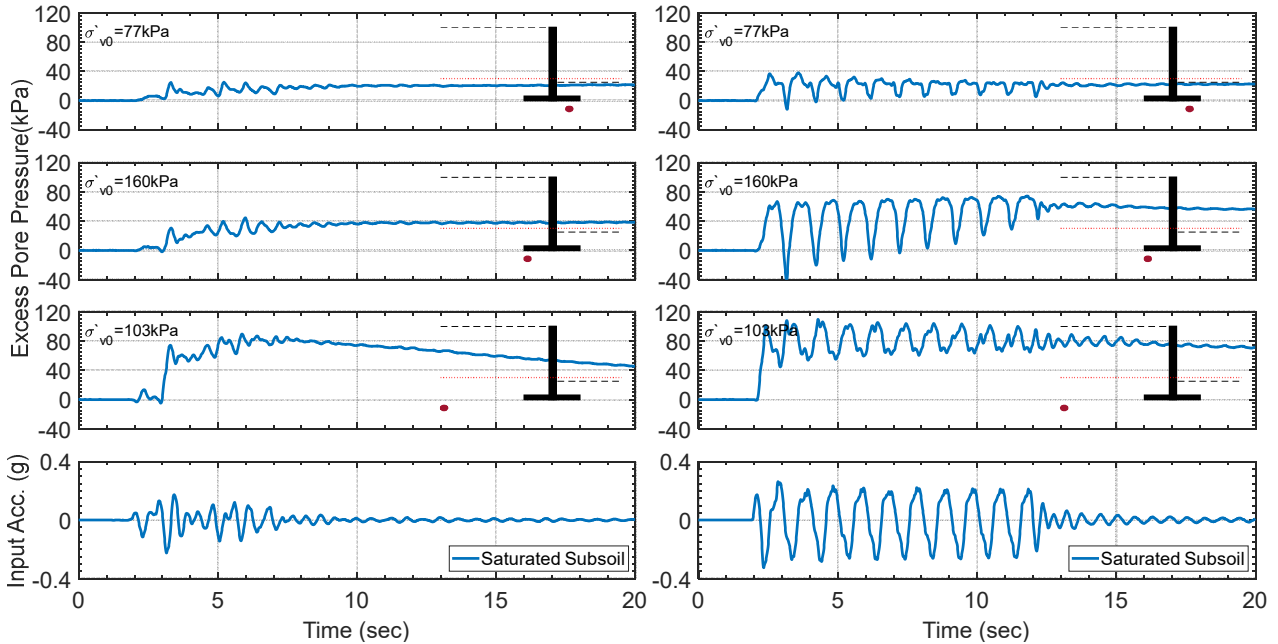

Figure 6. Co-seismic excess pore pressures recorded in the saturated soil model in two regions, free and near fields

induced bedrock motions, the positive acceleration means the abutment is driven towards the backfill.

For the dry soil model, acceleration amplification can be observed for the soil-abutment system during the vertical transmission of shear waves, and relative phase lags rise with the abutment height are proportional to the relative stiffness. For both earthquakes, the amplification of soil acceleration in the near field is higher than the free field due to the introduced additional kinematic loads resulting from the relative abutment-soil displacements, and inertial loads due to the soil-abutment mass difference. The kinematic loads are referred to different abutment and soil stiffnesses, while inertial loads since they have uneven masses. Further, the soil response to the high-frequency Kobe earthquake (left-hand side column) is relatively higher than the low-frequency sinusoidal motion (right-hand side column) by comparing the PGA; this might be because the former is close to the natural soil frequency (2.2-2.4 Hz) according to the shear wave velocity recorded by the air-hammer tool.

The accelerations are intimately linked to forces induced on the abutment and soil body and their movement magnitudes. The small relative soil-abutment acceleration provides a clue about how small the relative soil-abutment is. The relative movement, not the absolute, is the primary source of the forces exerted on abutments. The subsoil stiffness is crucial in governing the overall deformation mechanism and response.
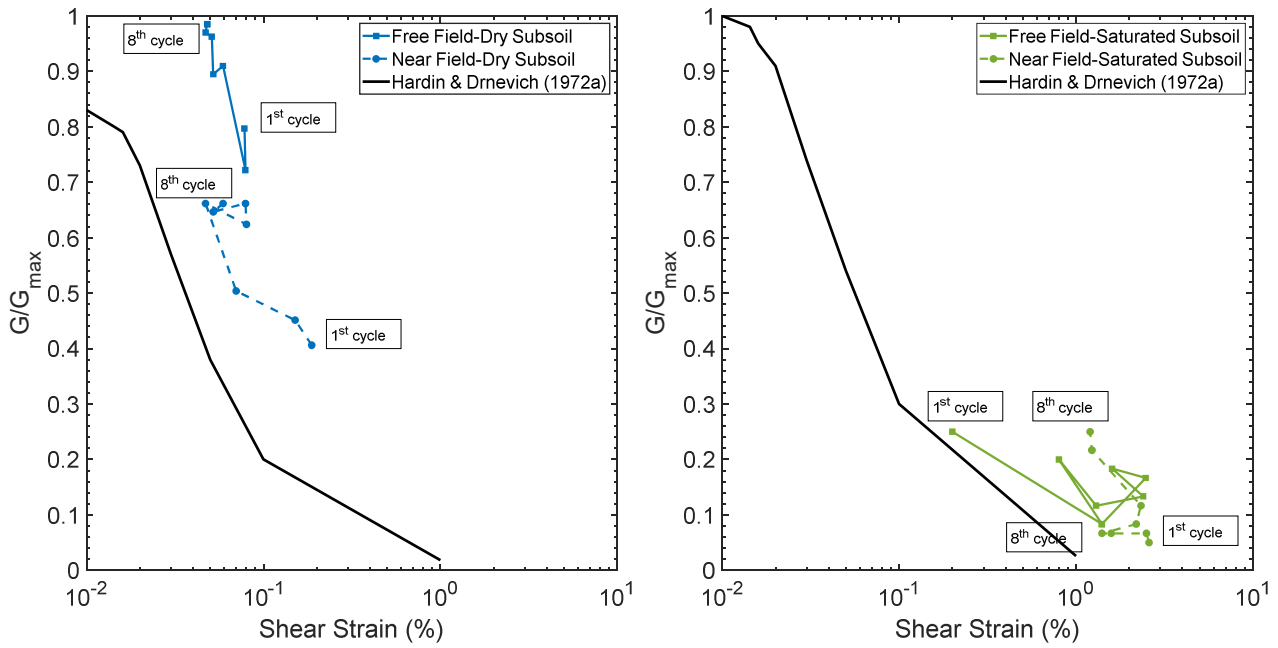
Figure 7. Shear modulus variation of dry and saturated sandy soil models

Observing small relative soil-wall movement compares well with the evaluated soil stiffness, as shown in Fig. 7. For the dry soil model condition, fairly consistent cyclic soil stiffness variations at later cycles of the input motion compared to the gradual soil hardening in the first three cycles in the near field area. On the other hand, steep soil hardening can be seen in the free field zone. Furthermore, the volumetric contractile strain in the free field is lower than the near field area surrounding the abutment footing. That is due to the variation soil confining stresses and induced-shear stresses at the different locations of the same depth, which in turn cause higher volumetric strain underneath the abutment, lowering the soil shear modulus. It is worth highlighting that the obtained shear strains from the double integration of soil accelerations histories are comparable with the shear strain values measured by the GeoPIV-RG image analysis though not presented in this paper, and the soil stiffness values agree with the ones obtained from the air-hammer tool. The shear wave velocity in the free and near fields was 270 m/s and 186 m/s, respectively. Thus, the soil modulus before the input motion of the ten cycles sinusoidal wave was 108 and 52 MPa. Normalising these values with the maximum soil stiffness shown in Table 3 verifies the competence of stress-strain loops constructed from the soil acceleration histories for the dry soil model test.

Concerning the dynamic soil and abutment behaviour in the saturated soil model configuration. Fig. 5 compares the seismic soil behaviour in the free and near fields for both earthquakes, scaled Kobe and sinusoidal waves. The relative abutment acceleration is also presented. The interpretation of soil and abutment accelerations histories will be directly compared with the generated excess pore pressure time histories, as shown in Fig. 6. The initial vertical effective stresses at each depth, hand-calculated, are also outlined. They are approximate values, and the uplift force following the positive pore pressure generation is not deducted from the abutment-bearing pressure. Furthermore, the recent proposal regarding the

dynamic variation of the vertical effective stresses along a horizontal plane that accounts for the earth pressure changes, is also not considered in this research (Madabhushi and Haigh 2022). The latter novel point would alter the definition of soil liquefaction as the mean confining stresses depends on both vertical and horizontal effective stresses; soil liquefies when the positive excess pore pressure matches the initial mean confining stress p_o (i.e., r_u=1 condition). Instead, the generated positive excess pore pressure should be compared to the current mean confining stress p_c at any given time instant.

The positive excess pore pressures from the scaled Kobe earthquake (left-hand side column) are relatively large and adequate to liquefy the soil, as shown in Fig. 6. The initial increase in the excess pore pressure indicates the overall contractile tendency of soil. The subsequent soil dilative behaviour observed as a cyclic drop of excess pore pressure shows that the induced input motion was enough to liquify the soil in the free and near fields fully. The soil stiffness reduction underneath the abutment is coupled with a downward movement of the abutment. At the same time, the attenuation of positive soil accelerations in the near and far fields are prominent. The near-zero effective confining stresses limit the soil's ability to transmit shear stresses. This is evidence that the liquefaction phenomenon has been triggered, although the calculated initial vertical effective stresses indicate that the soil still has a significant stiffness, justifying the inappropriate definition of liquefaction (r_u=1). Furthermore, the free and near field zones experience volumetric contractile behaviour when the abutment is driven towards the retained soil. Also, the relative excess pore pressure build-up underneath the abutment can be seen due to a relative subsoil volumetric contraction. The reduction of soil stiffness has considerably affected the dynamic abutment response. The peak acceleration of the abutment is nearly double that PGA of the input motion. That is attributed to the degradation of subsoil stiffness following the generated positive excess pore pressure and

hence lower soil damping. Simultaneously, the stiff abutment interacts with the localised yielding soil, lower inertial interaction effects at the subsoil-abutment interface, therefore lower radiation damping.

On the other hand, the overall system response to the ten cycles of sinusoidal input motion is remarkably different, as shown in Fig. 6 (right-hand side column). When the abutment is driven towards the backfill, soil softening can be seen in the free field area following the positive excess pore pressure generation. In contrast, soil hardening behaviour is underneath the abutment correlating with the negative excess pore pressure. The shear-induced dilation in this earthquake is considerably higher than the scaled Kobe ground motion. Consequently, large co-seismic suction spikes can overcome the volumetric contraction behaviour of the dry backfill soil. By looking at the corresponding soil accelerations for this earthquake in the right-hand side column of Fig. 5, the spikes of positive soil accelerations are apparent in the near field following the suction pressures. As a result of high shear stresses, soil dilates and hence significant acceleration. Similarly, the attenuation of negative soil acceleration is apparent due to the soil stiffness reduction following the positive excess pore pressure generation by comparing the near-field results shown in Fig. 5 and Fig. 6. However, surprisingly, although the soil in the free field has liquified following the positive excess pore pressure, the attenuation of positive soil acceleration is barely manifest; this might be because the dry backfill soil governs the movement of the close saturated soil layer.

Similar volumetric deformation behaviour observed in the scald Kobe earthquake can also be seen underneath the abutment following the sine wave motion. The different generated excess pore pressure underneath the left and right-hand side of the abutment footing indicates the mode movement of the abutment, cyclic rotation movement. The relative excess pore pressure values might be attributed to the different overburden stresses at both sides of the abutment and the witnessed soil flow mechanism. The backfill soil streamed from the left-hand side of the abutment to the right-hand side of the abutment during the earthquake for equilibrium, hence higher lateral soil stresses. However, the experienced rotational movement still exceeds the serviceability limit state (SLS). Hence earthquake-induced liquefaction failure for the abutment constructed over liquifiable subsoil. The rotational movement of the abutment can be visualised from the mid and top-abutment acceleration traces. The gradual reduction of positive abutment acceleration proves that the MEMS instrument has already started reading the centrifugal acceleration beside the shaking movement due to the abutment rotation.

Comparing the soil acceleration underneath the abutment and the abutment acceleration indicate that both are approximately in phase movement but by different magnitudes. When the wall is driven towards the backfill, its acceleration is less than the soil, meaning that an opening up of the abutment around the top support, which occurred during the active-abutment movement, is not completely reversed in the next half cycle (passive-abutment movement). The dry backfill

movement and the induced lateral stresses govern the outward rotation of the abutment.

The soil stiffness values obtained from the stress-strain loops for the saturated soil model test, as shown in Fig. 7, also show the remarkable soil stiffness degradation in the free field while soil stiffening for the subsoil underneath the abutment. The massive soil stiffness degradation from the first cycle compares well with the generated positive excess pore pressure shown in Fig. 6 (right-hand side). The generated negative positive excess pore pressure when the abutment moves towards the backfill stiffens the soil underneath the abutment temporarily before reversing the load and driving the abutment away from the backfill, which generates positive excess pore pressure and attenuates the soil acceleration due to the soil volumetric contraction. Therefore, one representative soil stiffness value during one complete cycle is hard to be obtained from liquefiable sandy soil. Comparing the soil stiffness values with corresponding shear strains does not provide a clear idea of the dilative and contractile soil behaviour during each complete cycle. Therefore, processing the excess pore pressure against the soil stiffness or calculating the soil stiffness for each half-cycle would be better since it could provide the soil stiffness variation correlated with the soil volumetric expansion and contraction for each half-cycle.

5. Conclusions

Integral abutment bridges (IABs) are increasingly attractive to transport agencies as an alternative scheme to conventional bridges.

Two centrifuge tests have been utilised to understand the subsoil stiffness effects governing the abutment movement mode and magnitude. The experimental tests had similar configurations, with the only difference being dry subsoil in one test and saturated subsoil in the other. The water table level surrounded the abutment footing, representing the case of a bridge crossing a river.

The bridge deck simulation was by a prop allowing rotational and vertical movement only. Although this does not replicate the rigid connection of IBs, these tests will better understand how the rigid connection would alter the soil deformation mechanism and the earth pressure build-up behind abutments.

In the dry soil model test, subsoil hardening behaviour was observed during the cyclic motion, indicative of the locked-in stresses, hence reducing the relative soil-abutment movement and governing the movement to be dominantly translational. In contrast, the remarkable subsoil stiffness degradation following positive excess pore pressure generation induced severe rotational movement, exceeding the SLS and earthquake-induced liquefaction failure. The ratcheting mechanism of the abutment rotation was identified based on the measurements of different instrumentation techniques. In each half-cycle of the input motion, the abutment is displaced and rotated away from the backfill. Still, this movement was partially recovered in the other half-cycle of acceleration.

Acknowledgements

References

Burke, Jr., P., Martin. "Integral and semi-integral bridges". John Wiley & Sons, 2009.

Brennan, A. J., N. I., Thusyanthan, and S. P., Madabhushi.. "Evaluation of shear modulus and damping in dynamic centrifuge tests." Journal of geotechnical and geoenvironmental engineering 131, no. 12, 2005. https://doi.org/10.1061/(ASCE)10900241(2005)131:12(1488).

Erhan, S., and M. Dicleli"Effect of dynamic soil–bridge interaction modeling assumptions on the calculated seismic response of integral bridges." Soil Dynamics and Earthquake Engineering 66,. 2014. https://doi.org/10.1016/j.soildyn.2014.06.033

Haigh, S. K., J., Eadington, and S. P. G., Madabhushi. 2012. "Permeability and stiffness of sands at very low effective stresses." Géotechnique 62, 2012. https://doi.org/10.1680/geot.10.P.035.

Hardin, B. O., and V. P., Drnevich. "Shear modulus and damping in soils: design equations and curves." Journal of the Soil mechanics and Foundations Division 98, no. 7, 1972a. https://doi.org/10.1061/JSFEAQ.0001760.

Hardin, B. O., and V. P., Drnevich.. "Shear modulus and damping in soils: measurement and parameter effects (terzaghi leture)." Journal of the soil mechanics and foundations division 98, no. 6, 1972b. https://doi.org/10.1061/JSFEAQ.0001756.

Ghosh, B., and S. P. G., Madabhushi. "An efficient tool for measuring shear wave velocity in the centrifuge." In Physical modelling in geotechnics, 2022. https://doi.org/10.1201/9780203743362.

Kunin, J., and S., Alampalli "Integral abutment bridges: Current practice in United States and Canada." Journal of performance of constructed facilities 14, no. 3, 2000. https://doi.org/10.1061/(ASCE)0887-3828(2000)14:3(104).

Madabhushi, G. "Centrifuge modelling for civil engineers ". CRC press, 2014. https://doi.org/10.1201/9781315272863.

Madabhushi, S. P. G., N. E., Houghton, and S. K., Haigh. "A new automatic sand pourer for model preparation at University of Cambridge." In Proceedings of the 6th international conference on physical modelling in geotechnics, pp. 217-222. Taylor & Francis Group, London, UK, 2006.

Madabhushi, G. S., S. K., Haigh, N. E., Houghton, and E., Gould. "Development of a servo-hydraulic earthquake actuator for the Cambridge Turner beam centrifuge. "International Journal of Physical Modelling in Geotechnics 12, no. 2, 2012. https://doi.org/10.1680/ijpmg.11.00013.

Madabhushi, S. S., and S. K., Haigh.. "On the dynamic response of flexible dual-row retaining walls in dry sand." Géotechnique 72, no. 11, 2022 https://doi.org/10.1680/jgeot.19.P.189.

Mitoulis, S. A. "Challenges and opportunities for the application of integral abutment bridges in earthquake-prone areas: A review." Soil Dynamics and Earthquake Engineering 135, 2020. https://doi.org/10.1016/j.soildyn.2020.106183.

Schofield, A. N. "Cambridge geotechnical centrifuge operations." Geotechnique 30, no. 3, 1980. https://doi.org/10.1680/geot.1980.30.3.227.

Shepley, P. "Water injection to assist pile jacking." PhD diss., University of Cambridge. 2014.

Steedman, R. S., and S. P. G., Madabhushi. "Wave propagation in sand medium". University of Cambridge, Department of Engineering, 1990.

Stewart, D. P., Y. R., Chen, and B. L., Kutter. "Experience with the use of methylcellulose as a viscous pore fluid in centrifuge models." Geotechnical Testing Journal 21, no. 4, 1998, https://doi.org/10.1520/GTJ11376J.

Stringer, M. E., and S. P. G., Madabhushi. "Novel computer-controlled saturation of dynamic centrifuge models using high viscosity fluids." Geotechnical Testing Journal 32, no. 6, 2009. https://doi.org/10.1520/GTJ11376J.

Tubaldi, E., S. A., Mitoulis, and H. Ahmadi. "Comparison of different models for high damping rubber bearings in seismically isolated bridges." Soil Dynamics and Earthquake Engineering 104, 2018. https://doi.org/10.1016/j.soildyn.2017.09.017.

Zeghal, M., A. W., Elgamal, H. T., Tang, and J. C., Stepp. "Lotung downhole array. II: Evaluation of soil nonlinear properties." Journal of geotechnical engineering 121, no. 4, 1995. https://doi.org/10.1061/(ASCE)0733-9410(1995)121:4(363).